Geophysical Research Letters®

AGU ADVANCING EARTH AND SPACE SCIENCE

Learning by Doing: Seasonal and Diurnal Features of Tropical Precipitation in a Global-Coupled Storm-Resolving Model

H. Segura[1] ⓘ**, C. Hohenegger[1]** ⓘ**, C. Wengel[1], and B. Stevens[1]** ⓘ

[1]Max Planck Institute for Meteorology, Hamburg, Germany

Abstract Using the global and coupled ICOsahedral Nonhydrostatic model with the Sapphire configuration (ICON-S) and a grid spacing of 5 km, we describe seasonal and diurnal features of the tropical rainbelt and assess the limits of ICON-S in representing tropical precipitation. ICON-S shows that, by resolving meso-beta scale process, the rainbelt structure and its seasonality (zonal and meridional migration and enlargement) is reproduced, with better performance over land than over ocean and with a very high degree of agreement to observations. ICON-S especially struggles in capturing the seasonal features of the tropical rainbelt over the oceans of the Eastern Hemisphere, an issue associated with a cold sea surface temperature (SST) bias at the equator. ICON-S also shows that a perfect representation of the diurnal cycle of precipitation over land is not a requirement to capture the seasonal features of the rainbelt over land, while over the ocean, 5 km is sufficient to adequately represent the diurnal cycle of precipitation.

Plain Language Summary Over the tropics, precipitation falls in distinct bands, that span the circumference of the Earth. These bands migrate from the Northern to the Southern Hemisphere and vice versa following the seasonal migration of the sun. Their center of mass also varies east-west, as well as their area. Where rain ends up falling is of key importance but conventional climate models relying on statistical approaches to simulate convection cannot represent these characteristics. Here we report on the results of simulations on a global domain and, to our knowledge, for the first time integrated with an atmosphere-ocean coupled over a full seasonal cycle and with a grid spacing fine enough to explicitly represent convection and Mesoscale Ocean eddies. We show that such simulations can reproduce many aspects of the seasonal migration of the rainbelt over land. For instance, the north-south and east-west migration of the rainbelt as well as its expansion during the summer season are well captured. This is also the case for the rainbelt in the eastern Pacific and the Atlantic, but not in the Eastern Hemisphere, where the poor representation of the sea surface temperature pattern distorts the representation of the rainbelt and its seasonal characteristics.

1. Introduction

Storm-resolving models (SRMs) differ from traditional climate models through their explicit representation of fluid dynamical processes on the scale of a few, to a few tens, of kilometers. Motions on these scales, referred to as the meso-beta scale, shape the dynamics of convective precipitation—one of the climate system's most important processes. Decades of experience with regional models designed to simulate meso-beta scale processes (Baldauf et al., 2011; Done et al., 2004; Grell et al., 2000; Hohenegger et al., 2008; Prein et al., 2013), suggest that the emerging capability to also explicitly represent such processes on global domains (Dirmeyer et al., 2012; Miura, Satoh, Nasuno, et al., 2007; Miura, Satoh, Tomita, et al., 2007; Satoh et al., 2017; Stevens et al., 2020) will lead to more physical and more useful simulations of the Earth-system as a whole (Slingo et al., 2022).

The advantages of explicitly representing, rather than parameterizing convection are amply documented (Marsham et al., 2013; Satoh et al., 2019; Schär et al., 2020), justifying the excitement of using global SRMs (GSRMs) to represent the climate system. However, maximizing the potential of GSRMs will require effort. There is little literature on the use of SRMs coupled to fully interactive ocean over regional domains, questioning if the representation of meso-beta scale processes is enough to get the correct sea surface temperature (SST) structure, and in the end, the correct precipitation pattern. Over land, the good performance of SRMs with inter-active land surface on regional domains, as seen in past studies, raises the question whether this performance is a result of resolving processes or an imprint of the boundary conditions. To gain insight into those enigmas it is tempting to compromise resolution for throughput, with consequences for simulation fidelity. While the impact

of such trade-offs has been demonstrated for case studies of isolated systems (Marsham et al., 2013; Pearson et al., 2014; Prein et al., 2013), their effects globally are far from clear.

These issues motivate the present study, which analyzes the behavior of the coupled system when allowing for an explicit, albeit coarse, representation of meso-beta scale processes for an entire annual cycle. The simulations are performed using the ICOsahedral Nonhydrostatic (ICON) model with a horizontal grid spacing of 5 km across all components (Hohenegger et al., 2022). These are, to our knowledge, the first simulations of their kind, also meaning that the model system is still in an early stage of its development, leading to a greater potential for errors and imbalances. Our intention is, in trying to develop a more physical model, to learn more about how the system works, a form of learning by doing. Identifying what the simulations represent poorly helps target efforts to find implementation errors and to understand to what extent errors generalize. Together with an identification of what the simulations get right, even at their more marginal resolution, this allows a better assessment of the trade offs between resolution and throughput.

Specifically we investigate which aspects of the diurnal and, for the first time, the seasonal cycle of tropical precipitation are (or are not) reproduced by a 5 km mesh coupled GSRM. This focus was chosen because such cycles represent the most important responses of the climate to the solar forcing. By comparing our results to published works on the representation of precipitation over land using SRMs over regional domains and over ocean with fixed SST, we can further draw inferences as to the importance of explicitly resolving convective processes versus the specification of the underlying surface versus constraints on the large-scale flow. Our analysis of the seasonal cycle goes beyond a simple bias analysis, to additionally describe the seasonal evolution of the tropical rainbelt using an object based analysis. This allows to explore the sensitivity of the annual cycle of tropical precipitation to developing SST biases (irrespective of their source) as these are expected to couple to planetary scale energy transports (Adam et al., 2016; Schneider et al., 2014) to which the convection may be sensitive. Our analysis of the diurnal cycle of precipitation serves as a reference point for the representation of small-scale processes, and allows to address the impact of the representation of this variability on the seasonal features of tropical rainbelts.

2. Methods

2.1. ICON-Sapphire

We analyze simulations from a new ICON configuration, called Sapphire (Hohenegger et al., 2022), or ICON-S. ICON-S targets the representation of kilometer-scale processes across all components of the Earth system. We analyze the G_AO_5 km simulation described by Hohenegger et al. (2022), which employs a grid spacing of 5 km and 90 vertical levels in the atmosphere, 128 levels in the ocean and five soil layers. The simulation is started using the Integrated Forecasting System analysis from 20 January 2020, and is run until 28 February 2021.

Precipitation in ICON-S is interpolated to a regular grid of $0.1° \times 0.1°$. To allow a spin-up of the smaller scales of motion, the first 11 days of the simulation are discarded. To analyze the seasonal cycle, monthly means are calculated from February 2020 to January 2021. For the diurnal cycle analysis, hourly precipitation for February 2020 is used because we do not expect the mean diurnal cycle over land and over ocean to show much seasonality (see Yang & Slingo, 2001).

2.2. GPM Data

We use the IMERG V06 data set (Huffman et al., 2019) for comparison to the ICON-S simulations. While initialized with conditions in 2020, ICON-S diverges to a different state because of the chaotic nature of the climate system. Thus, the use of the climatology of IMERG, rather than a particular year, to compare the annual mean and the seasonal cycle of precipitation in ICON-S is a reasonable option. As a further check, we will investigate whether uncovered biases can be explained by internal variability. The climatology of IMERG is computed from monthly mean data for the period between January 2001 and January 2021. The diurnal precipitation cycle from IMERG is analyzed for the same period as for ICON-S, using hourly data.

2.3. SAL Method

To quantify and compare the seasonal evolution of the simulated tropical rainbelt with that inferred from observations, we make use of the Structure-Amplitude-Location (SAL) method (Wernli et al., 2008). The SAL method segments continuous grid cells where the value of precipitation is greater than a threshold that is chosen during the analysis. The resulting objects are then quantified in terms of their structure, amplitude, and location. Precipitation objects are calculated for different regions within the tropics (30°S–30°N) using monthly mean precipitation and making a distinction between ocean and land. The tropical rainbelt is defined as the precipitation object holding the largest area in each region (see Figure S1 in Supporting Information S1 as example). We are aware that by using this methodology, we can not properly characterize the finest structure of the tropical rainbelt, but as our objective is to analyze the seasonal changes and not the intraseasonal or day-to-day variations, we consider this approach valid. Moreover, the SAL method has proven useful in several studies analyzing the Intertropical Convergence Zone (ITCZ) and monsoon regions (Hohenegger & Stevens, 2013; Siongco et al., 2015, 2017).

3. Tropical Precipitation

3.1. The Annual Mean Structure

Figure 1a shows that ICON-S can represent the annual mean structure of tropical precipitation (see Figure S2 in Supporting Information S1), in particular the location of convective regions, enclosed by the quantile 80 (q80). A highly similar structure between ICON-S and the climatology of IMERG is notably observed in regions between the central Pacific and western Africa. Discrepancies are largest in the vicinity of the maritime continent. This is evident when calculating the percentage of grid cells in ICON-S inside the q80 contour that matches IMERG, being higher in the Western Hemisphere (180°W–0°E), with values around 73%, than in the Eastern hemisphere (47%).

There are three biases that stand out, the double precipitation band in the Indo-Pacific region, the more zonally elongated Southern Pacific Convergence Zone, and the signature of a double ITCZ in the eastern Pacific. A calculation of the index used by Samanta et al. (2019) to quantify the double ITCZ in the central Pacific gives a value of six (6), three times more than in observational data sets (Fiedler et al., 2020). Because individual years in IMERG do not sample the extreme values found in this analysis or the double precipitation band in the Indo-Pacific, we interpret these features as biases in ICON-S. In those regions, the annual structure of SST is not correctly represented, with a strong cold bias at the equator. Although the cold temperature cannot be explained by internal variability, the resulting SST zonal gradient in the Pacific looks similar to an El Niño year. Nevertheless, this similarity is not observed in the precipitation distribution (see Figure S3 in Supporting Information S1), confirming that it is a true model bias.

The mean tropical precipitation in ICON-S is 3.7 mm d^{-1}, 0.1 mm d^{-1} larger than the wettest year of IMERG (Figure S4 in Supporting Information S1). Part of this overestimation might be due to satellite observations underestimating precipitation (Bulovic et al., 2020; Lu & Yong, 2018; Pfeifroth et al., 2013), but the ICON dynamics also leaks energy (Gassmann, 2013), causing the atmosphere to cool more than would be expected based on its radiative cooling, which would otherwise constrain the rate of precipitation. The bias is higher over land (0.5 mm d^{-1}) than over ocean (0.2 mm d^{-1}). ICON-S reproduces the partitioning of precipitation between land and ocean, which is close to one in observation as documented by Hohenegger and Stevens (2022), a feature that models using parameterized convection cannot capture (Hohenegger & Stevens, 2022).

3.2. Summer-Winter Amplitude and Diurnal Cycle

ICON-S also reproduces the pattern of the seasonal difference in precipitation between the austral and boreal summer observed in the climatology of IMERG (Figure 1b, Figure S5 in Supporting Information S1). Among the characteristics that ICON-S reproduces are the seasonal location of convective regions (marked by the value of ±3 mm d^{-1}), the poleward extension of the convective regions over land and over the Indo-Pacific warm pool in their respective summer season, and a wider convective region in the Northern than in the Southern Hemisphere over the eastern Pacific and the Atlantic. However, ICON-S simulates a too large amplitude of the seasonal cycle over the equatorial Indian Ocean. The differences with IMERG persist when comparing to individual years, suggesting a systematic bias in ICON-S (see Figure S6 in Supporting Information S1). Moreover, the internal
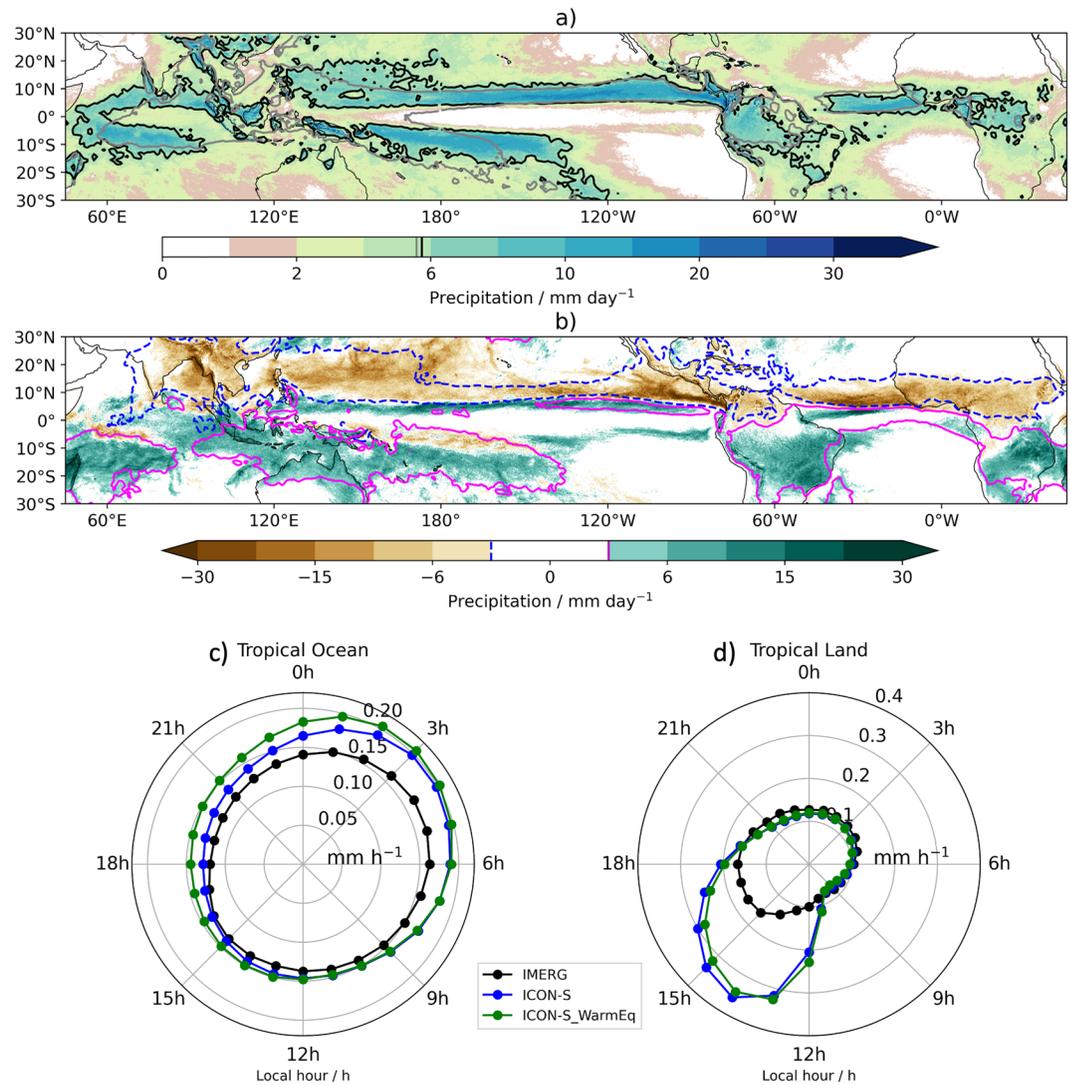
Figure 1. (a) Annual mean precipitation in ICOsahedral Nonhydrostatic model with the Sapphire configuration (ICON-S; January 2020–February 2021; shaded). The quantile 80 of the annual mean of both ICON-S (black contour) and the climatology of IMERG (2001–2020; gray contour) are shown. (b) January–February 2021 minus August–September 2020 precipitation in ICON-S (shaded). In IMERG, the climatology of both seasons is used and only the contour lines of 3 mm d^{-1} (magenta) and −3 mm d^{-1} (blue) are plotted. In (a, b), the values of the contours are indicated in the colorbar. (c, d) Clock diagram of the diurnal cycle of precipitation over the tropical ocean and the tropical land, respectively, for February 2020. The angles represent the local hour and the radius the intensity. IMERG, ICON-S, and ICON-S_WarmEq are represented by a black, blue, and green line, respectively.

variability of the summer-winter amplitude in IMERG displays a robust spatial structure across the years over land, the eastern Pacific, and the Atlantic, but not in the Eastern Hemisphere. This indicates that regions where the signal of the seasonal cycle is much larger than that of interannual variability are regions, whose precipitation seasonality should be correctly simulated by climate models, as ICON-S does.

Tropical precipitation is also characterized by its specific diurnal cycle. Figures 1c and 1d shows the mean diurnal cycle of precipitation in each grid cell averaged over the ocean and land, respectively. As in IMERG, ICON-S displays a peak in the early morning over the ocean. Over the land, ICON-S and IMERG show the expected afternoon strong diurnal peak, but differences exist. ICON-S shows a diurnal cycle with a precipitation peak of ∼0.37 mm hr^{-1} occurring between 13 and 15 LT, twice more intense and two hours earlier than in IMERG. Some studies noted a similarly too pronounced diurnal cycle based on simulations using 2–4 km grid spacing (Argüeso et al., 2020; Arnold et al., 2020; Marsham et al., 2013), similar to what we find here. There is evidence
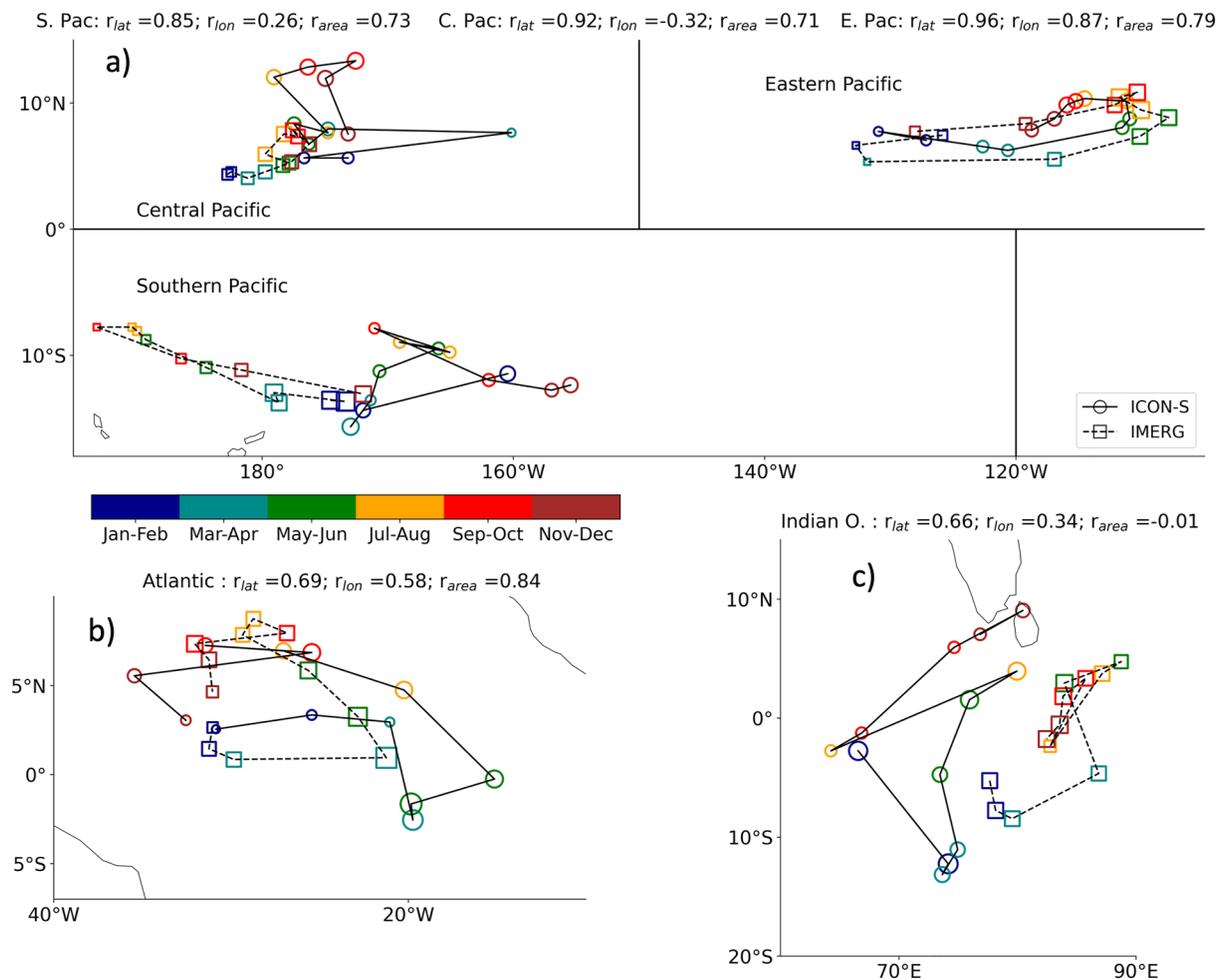
Figure 2. Monthly mean location of the centroid of the rainbelt over the tropical ocean calculated by using the SAL method from ICOsahedral Nonhydrostatic model with the Sapphire configuration (ICON-S) (circles and solid lines) and IMERG (squares and dashed lines). Marker colors indicate the month and for a better visualization, colors are grouped by 2 months. Marker size represents the ratio between the area of the rainbelt in each month compared to the annual mean. (a) the eastern Pacific (0°N–20°N; 150°W–80°W), the central Pacific (0°N–20°N; 160°E–150°W), the Southern Pacific (20°S–0°N; 160°E–150°W), (b) the Atlantic Ocean (60°W–10°E; 10°S–20°N), (c) the Indian Ocean (50°E–105°E; 30°S–30°N). The correlation values between ICON-S and IMERG for the longitude and latitude of the centroid and its area are shown in the upper part of each subplot.

of a reduction of these biases with finer resolution, perhaps through an ability to partially resolve subcloud layer circulations (see Petch et al., 2002). For instance, the simulations described by Stevens et al. (2020), which employed grid spacings of 1 km and finer, reproduced correctly the amplitude of the diurnal cycle over Germany.

4. The Ocean Rainbelt

Using monthly mean precipitation from ICON-S and the monthly mean climatology of IMERG, we define a rainbelt by computing for each month the 80% quantile of precipitation over the entire tropical ocean. After masking grid cells that fall below this value, we divide the tropical ocean in five regions, the tropical Atlantic, the eastern, central and southern Pacific and the Indian Ocean. In each region, we segment the remaining data and apply the SAL method to isolate the precipitation object with the maximum area. Only objects spanning a minimum area of 250,000 km^2 (roughly 5° × 5°) are retained and these are identified as the rainbelt of the respective ocean region. These form the basis for our further analysis of their structure (area) and location (centroid).

Figure 2 shows the seasonal movement and the change in the area of the rainbelt over the analyzed ocean regions. The agreement in the seasonal change of the location and the area of the rainbelt between ICON-S and IMERG is quantified by the correlation of the latitude (meridional migration), longitude (zonal migration), and area. In the

five regions, the rainbelt possesses both a meridional and zonal migration, which ICON-S can reproduce, but with less agreement in the zonal movement. The correlation between ICON-S and IMERG are larger than 0.65 in all regions regarding the meridional migration, while only the eastern Pacific and the Atlantic show correlation coefficients higher than 0.5 in the zonal migration. Over the central Pacific ICON-S reproduces an opposite seasonal change in the zonal migration and a more poleward migration. Over the southern Pacific, the most westward location of the rainbelt occurs in March in ICON-S, 7 months earlier than in IMERG. And there is an anomalous eastward migration of the rainbelt over the Indian Ocean.

IMERG also indicates changes in the rainbelt area in different ways across the different regions (Table S1 in Supporting Information S1). The maximum area of the rainbelts in the Pacific coincides with their most poleward location, occurring in their respective summer seasons. The Atlantic has a different dynamic, with the maximum area occurring in April–May. All the above characteristics are reproduced by ICON-S with correlation coefficients higher than 0.71, with the Atlantic holding the highest correlation ($r = 0.84$). In contrast, the low correlation value in the Indian Ocean is explained by the strongly seasonal areal change in the rainbelt simulated by ICON-S and not observed in IMERG. This is related to the splitting of the rainbelt displayed in Figure 1a.

Our results indirectly and mostly confirm the conclusion from past studies (Siongco et al., 2015; Wu et al., 2003) that convective parameterizations hamper the representation of many aspects of the rainbelt seasonality in the Eastern Pacific and the Atlantic. Nevertheless, ICON-S also has substantial precipitation biases in the Eastern Hemisphere, a region where the SST structure is not adequately represented (Figure S3 in Supporting Information S1). To what extent this SST bias pattern impacts the representation of tropical precipitation is discussed further in Sectoin 6.

5. The Rainbelt Over Land

To analyze the rainbelt over tropical land, we use the same methodology as for the tropical ocean. We apply this analysis in four regions, South America, Africa, India, and Southeast Asia. Figure 3 shows the seasonal migration and structural changes of the tropical rainbelt over land. In South America, the rainbelt reaches its southernmost position and shows its maximum extension during the austral summer (see Table S2 in Supporting Information S1), the core of the monsoon season. As compared to over the ocean, ICON-S reproduces the seasonal behavior of the rainbelt in South America surprisingly well, with high correlation values in the latitude (0.98), longitude (0.93), and area (0.96).

The rainbelt in Africa shows similar characteristics as in South America in its North-South migration, which is restricted to a latitude band between 15°S and 15°N. In Africa, the largest area of the rainbelt occurs toward the end of boreal summer. ICON-S captures the meridional migration of the African rainbelt ($r = 0.99$) but struggles in reproducing its seasonal areal changes. In particular, ICON-S does not reproduce the shrinking of the rainbelt in the May–July season, which explains the low correlation value ($r = 0.55$) and the positive bias of precipitation over central Africa observed in Figure 1a. IMERG also identifies a pronounced east-west migration of more than 20°. ICON-S generally reproduces this feature, modulo one outlier point, which explains the slightly low correlation value of 0.74.

Over the South Asia subcontinent a large-scale (>250,000 km^2) precipitation object is only observed from April to October for Southeast Asia and from June to October for India. Besides, both regions show a southward migration from the subtropics to 15°N. During its southward migration, the rainbelt over Southeast Asia expands, and its center of activity migrates from China to Myanmar, Thailand, and Laos. ICON-S reproduces the characteristics of the rainbelt in Southeast Asia, with correlation values in the latitude, longitude, and area of 0.97, 0.99, and 0.92, respectively. Over India, the SAL method only capture the rainbelt in ICON-S for 3 months (July–September), indicating a dry onset and demise of the rainbelt compared to IMERG. Thus, from a tropical perspective, ICON-S with a grid spacing of 5 km reproduces the different characteristics of the rainbelt over land despite distortions of the diurnal cycle of precipitation.
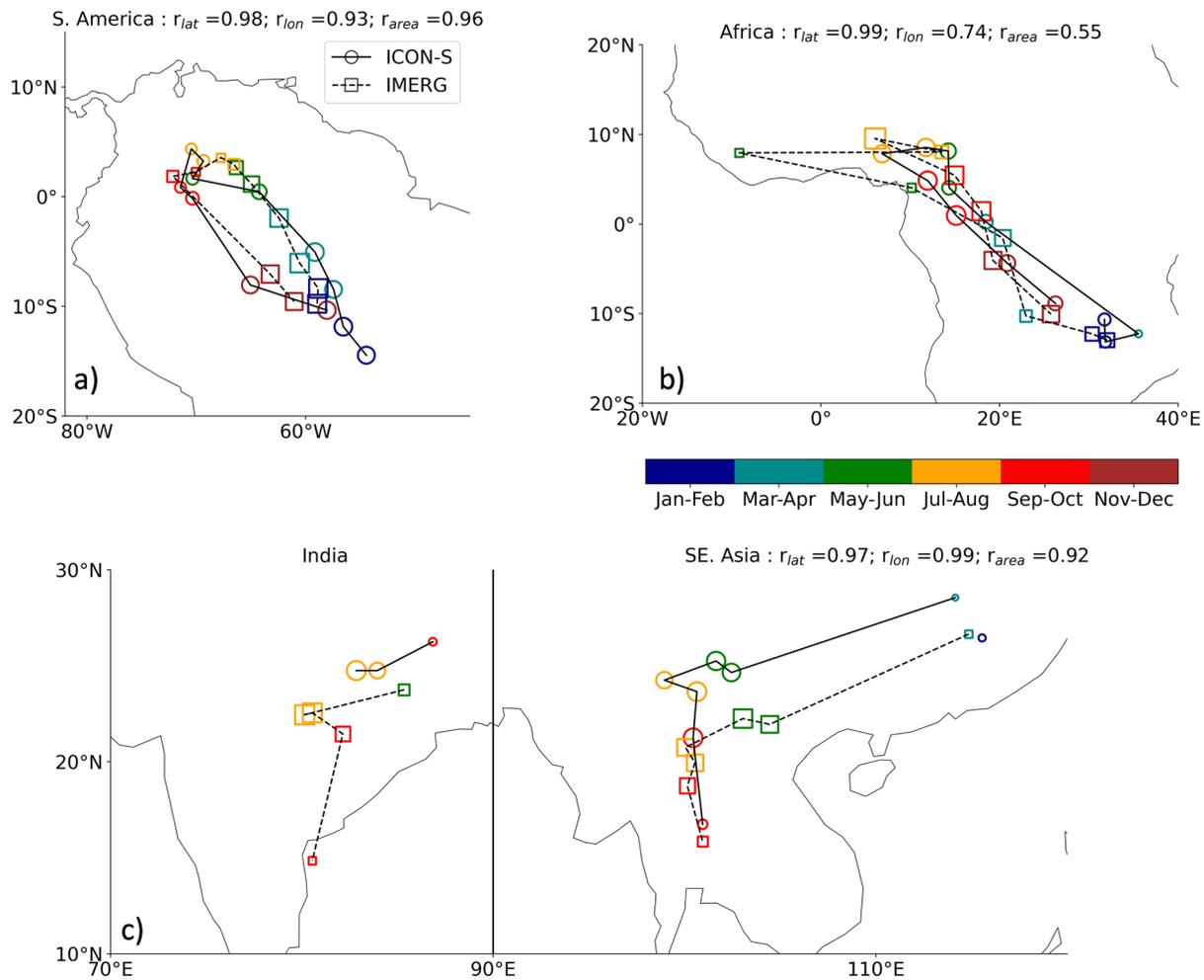
Figure 3. Similar to Figure 2, but only over the tropical land. (a) South America (82°W–30°W; 30°S–13°N), (b) Africa (20°W–45°E; 30°S–25°N), and (c) India (70°E–90°E; 10°N–30°N), and Southeast Asia (90°E–120°E; 10°N–30°N).

6. Changing SST Pattern

ICON-S has more difficulty in representing the structure and evolution of the tropical rainbelts over ocean than over land, questioning the role of SST bias in explaining these difficulties. During the model development cycle, a similar simulation as ICON-S was performed in which the momentum transfer from the atmosphere to the ocean was switched off to test the influence of the wind-driven circulations on the simulations. This leads to substantial changes in the pattern of SST that allowed us to gain insights into the impact of the SST pattern on the tropical precipitation structure. In this experiment, the equatorial region over ocean is characterized by a strong warming compared to ICON-S, and for this reason, we named this experiment ICON-S_WarmEq. Because it was used to test ocean coupling it also uses a different vertical coordinate system in the ocean (Z_*) together with different parameterizations (Table S3 in Supporting Information S1). It also covers a slightly different period, between 20 January 2020 and 20 September 2020.

Contrary to ICON-S, ICON-S_WarmEq produces an SST pattern with a less pronounced equatorial cold tongue (Figure 4, Figure S7 in Supporting Information S1). The impact of this SST pattern is particularly evident in the Indian Ocean, where a single band of precipitation is reproduced in ICON-S_WarmEq (not shown) and where the rainbelt presents similar seasonal characteristic as seen in observation ($r > 0.6$ in Figure 4). Moreover, the SST pattern in ICON-S_WarmEq is associated with a wet onset and demise of the Indian monsoon (Figure S8 in Supporting Information S1). In the other ocean regions, correlation values between ICON-S_WarmEq versus IMERG and ICON-S versus IMERG are similar (Figures 2 and 4), but the latitudinal range of the seasonal
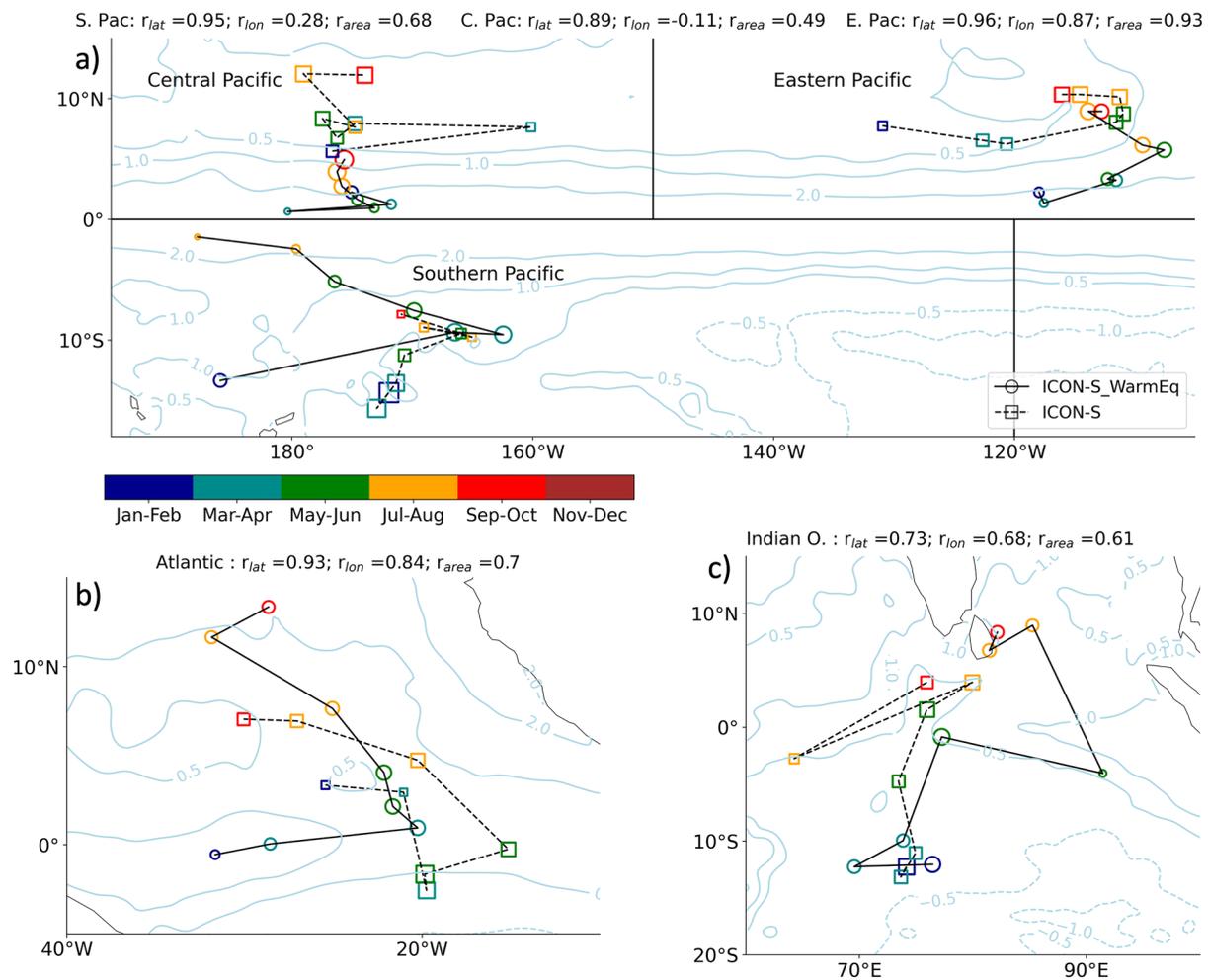
Figure 4. (a–c) Similar to Figure 2, but using ICOsahedral Nonhydrostatic model with the Sapphire configuration (ICON-S)_WarmEq (circles and solid lines) and ICON-S (squares and dashed lines) and between 1 February and 22 September 2020. The sea surface temperature (SST) difference between ICON-S_WarmEq and ICON-S is shown. Positive (negative) values are plotted in solid (dashed) contours and the contour line of 0 K is omitted. SST is interpolated to a resolution of 0.25°. The correlation values in the upper part of each panel are calculated between IMERG and ICON-S_WarmEq.

migration changes. The no simulation of the cold bias at the equator (Figures S3 and S7 in Supporting Information S1) constrains the poleward migration of the rainbelt in the central Pacific. This analysis points to SST biases as the explanation for the misrepresentation of the tropical rainbelts by ICON-S in the Eastern Hemisphere. As expected changes in SSTs do not impact the diurnal cycle of precipitation (Figures 1c and 1d).

7. Concluding Thoughts

ICON-S run in a global and coupled set-up produced many encouraging, and some intriguing, results. The precipitation seasonality over land is well reproduced despite some biases in the diurnal cycle, but at least the remaining bias in peak time is strongly reduced compared to models using parameterized convection. Over the ocean, the picture is more complicated, but informative of some of the challenges lying ahead, as illustrated by the following line of reasoning.

Over land, the vast literature on regional SRMs linked improvements in the representation of precipitation to the explicit representation of meso-beta processes, such as cold pools (e.g., Marsham et al., 2013; Maurer et al., 2017), mesoscale convective systems (e.g., Becker & Hohenegger, 2021; Peters et al., 2019) as well as interactions with land surface features circulations (e.g., Birch et al., 2015; Grell et al., 2000; Hohenegger et al., 2008). Regional simulations are nevertheless constrained by the imposed flow at the boundary. The results of our global

simulations indicate that, even when the large-scale is not constrained and even in the presence of clear SST biases, explicitly resolving meso-beta scale processes seem sufficient to capture the main feature of precipitation over land.

Over an interactive ocean the representation of convection appears more challenging. While ICON-S appears to well represent the convective response to the SST pattern it simulates, the pattern of SSTs are out of sample in the Eastern Hemisphere. Whether the SST biases come from unresolved sub-grid processes in the atmosphere (e.g., overestimation of non-precipitating clouds) or in the ocean (e.g., vertical structure of the ocean) or remaining implementation errors is still unclear, but understanding those biases should guide future work.

The correct representation of the terrestrial rainbelt in ICON-S, even if the SST structure is not, and the small internal variability in the summer-winter precipitation amplitude over land in IMERG signals the existence of a mechanism over land, but not over ocean, that makes it easier to reproduce precipitation. One hypothesis is the existence of a negative feedback between soil moisture and precipitation, which homogenizes the precipitation distribution and dampens precipitation perturbations (see Hohenegger & Stevens, 2018). The misrepresentation of this mechanism in models using convective parameterization (Hohenegger et al., 2009) could have masked its role in regulating continental precipitation, a role that is now more apparent through the increased fidelity in the representation of convective processes. This points to the fact that GSRMs are not only tools for better climate projections, but efforts to identify the causes of their remaining biases provide new opportunities to understand the Earth System—something we call learning by doing.

Data Availability Statement

The ICON-S simulation were done with the ICON branch nextgems_cycle1_dpp0066 as commit 62dbfc. And the ICON-S_WarmEq were done with the ICON branch nextgems_cycle1_zstar as commit 32adb2, 83f3dc, c17dcc. The source code is available here https://doi.org/10.17617/3.1XTSR6. The ICON model is available to individuals under licenses (https://mpimet.mpg.de/en/science/modeling-with-icon/code-availability). The IMERG data (Huffman et al., 2019) was obtained from the Integrated Climate Data Center website https://www.cen.uni-hamburg.de/en/icdc/data/atmosphere/imerg-precipitation-amount.html and the HadISST data (Rayner et al., 2003) from the Integrated Climate Data Center website https://www.cen.uni-hamburg.de/en/icdc/data/ocean/hadisst1.html. The scripts used to process the data and to plot the figures in the paper can be found as supplementary material in the repository: https://hdl.handle.net/21.11116/0000-000B-4BAE-E.

References

Adam, O., Bischoff, T., & Schneider, T. (2016). Seasonal and interannual variations of the energy flux equator and ITCZ. Part I: Zonally averaged ITCZ position. *Journal of Climate*, *29*(9), 3219–3230. https://doi.org/10.1175/JCLI-D-15-0512.1

Argüeso, D., Romero, R., & Homar, V. (2020). Precipitation features of the maritime continent in parameterized and explicit convection models. *Journal of Climate*, *33*(6), 2449–2466. https://doi.org/10.1175/JCLI-D-19-0416.1

Arnold, N. P., Putman, W. M., & Freitas, S. R. (2020). Impact of resolution and parameterized convection on the diurnal cycle of precipitation in a global nonhydrostatic model. *Journal of the Meteorological Society of Japan*, *98*(6), 1279–1304. https://doi.org/10.2151/jmsj.2020-066

Baldauf, M., Seifert, A., Förstner, J., Majewski, D., Raschendorfer, M., & Reinhardt, T. (2011). Operational convective-scale numerical weather prediction with the COSMO model: Description and sensitivities. *Monthly Weather Review*, *139*(12), 3887–3905. https://doi.org/10.1175/MWR-D-10-05013.1

Becker, T., & Hohenegger, C. (2021). Entrainment and its dependency on environmental conditions and convective organization in convection-permitting simulations. *Monthly Weather Review*, *149*(2), 537–550. https://doi.org/10.1175/MWR-D-20-0229.1

Birch, C. E., Roberts, M. J., Garcia-Carreras, L., Ackerley, D., Reeder, M. J., Lock, A. P., & Schiemann, R. (2015). Sea-breeze dynamics and convection initiation: The influence of convective parameterization in weather and climate model biases. *Journal of Climate*, *28*(20), 8093–8108. https://doi.org/10.1175/JCLI-D-14-00850.1

Bulovic, N., McIntyre, N., & Johnson, F. (2020). Evaluation of imerg v05b 30-min rainfall estimates over the high-elevation tropical andes mountains. *Journal of Hydrometeorology*, *21*(12), 2875–2892. https://doi.org/10.1175/JHM-D-20-0114.1

Dirmeyer, P. A., Cash, B. A., Kinter, J. L., Jung, T., Marx, L., Satoh, M., et al. (2012). Simulating the diurnal cycle of rainfall in global climate models: Resolution versus parameterization. *Climate Dynamics*, *39*(1–2), 399–418. https://doi.org/10.1007/s00382-011-1127-9

Done, J., Davis, C. A., & Weisman, M. (2004). The next generation of NWP: Explicit forecasts of convection using the weather research and forecasting (WRF) model. *Atmospheric Science Letters*, *5*(6), 110–117. https://doi.org/10.1002/asl.72

Fiedler, S., Crueger, T., D'Agostino, R., Peters, K., Becker, T., Leutwyler, D., et al. (2020). Simulated tropical precipitation assessed across three major phases of the coupled model intercomparison project (CMIP). *Monthly Weather Review*, *148*(9), 3653–3680. https://doi.org/10.1175/MWR-D-19-0404.1

Gassmann, A. (2013). A global hexagonal C-grid non-hydrostatic dynamical core (ICON-IAP) designed for energetic consistency. *Quarterly Journal of the Royal Meteorological Society*, *139*(670), 152–175. https://doi.org/10.1002/qj.1960

Grell, G. A., Schade, L., Knoche, R., Pfeiffer, A., & Egger, J. (2000). Nonhydrostatic climate simulations of precipitation over complex terrain. *Journal of Geophysical Research*, *105*(D24), 29595–29608. https://doi.org/10.1029/2000JD900445

Hohenegger, C., Brockhaus, P., Bretherton, C. S., & Schär, C. (2009). The soil moisture-precipitation feedback in simulations with explicit and parameterized convection. *Journal of Climate*, *22*(19), 5003–5020. https://doi.org/10.1175/2009JCLI2604.1

Hohenegger, C., Brockhaus, P., & Schär, C. (2008). Towards climate simulations at cloud-resolving scales. *Meteorologische Zeitschrift*, *17*(4), 383–394. https://doi.org/10.1127/0941-2948/2008/0303

Hohenegger, C., Korn, P., Linardakis, L., Redler, R., Schnur, R., Adamidis, P., et al. (2022). ICON-sapphire: Simulating the components of the Earth system and their interactions at kilometer and subkilometer scales. *Geoscientific Model Development Discussions*, *2022*, 1–42. https://doi.org/10.5194/gmd-2022-171

Hohenegger, C., & Stevens, B. (2013). Controls on and impacts of the diurnal cycle of deep convective precipitation. *Journal of Advances in Modeling Earth Systems*, *5*(4), 801–815. https://doi.org/10.1002/2012ms000216

Hohenegger, C., & Stevens, B. (2018). The role of the permanent wilting point in controlling the spatial distribution of precipitation. *Proceedings of the National Academy of Sciences of the United States of America*, *115*(22), 5692–5697. https://doi.org/10.1073/pnas.1718842115

Hohenegger, C., & Stevens, B. (2022). Tropical continents rainier than expected from geometrical constraints. *AGU Advances*, *3*(4), e2021AV000636. https://doi.org/10.1029/2021AV000636

Huffman, G., Stocker, E., Bolvin, D., Nelkin, E., & Tan, J. (2019). *GPM IMERG final precipitation L3 half hourly 0.1 degree x 0.1 degree V06 (Tech. Rep.)*. Goddard Earth Sciences Data and Information Services Center (GES DISC). distributed in netCDF file format by ICDC, CEN, University of Hamburg. https://doi.org/10.5067/GPM/IMERG/3B-HH/06

Lu, D., & Yong, B. (2018). Evaluation and hydrological utility of the latest GPM IMERG V5 and GSMaP V7 precipitation products over the Tibetan Plateau. *Remote Sensing*, *10*(12), 2022. https://doi.org/10.3390/rs10122022

Marsham, J. H., Dixon, N. S., Garcia-Carreras, L., Lister, G. M., Parker, D. J., Knippertz, P., & Birch, C. E. (2013). The role of moist convection in the West African monsoon system: Insights from continental-scale convection-permitting simulations. *Geophysical Research Letters*, *40*(9), 1843–1849. https://doi.org/10.1002/grl.50347

Maurer, V., Bischoff-Gauß, I., Kalthoff, N., Gantner, L., Roca, R., & Panitz, H. J. (2017). Initiation of deep convection in the Sahel in a convection-permitting climate simulation for northern Africa. *Quarterly Journal of the Royal Meteorological Society*, *143*(703), 806–816. https://doi.org/10.1002/qj.2966

Miura, H., Satoh, M., Nasuno, T., Akira, T. N., & Oouchi, K. (2007). A Madden-Julian oscillation event realistically simulated by a global cloud-resolving model. *Science*, *318*(5857), 1763–1765. https://doi.org/10.1126/science.1148443

Miura, H., Satoh, M., Tomita, H., Noda, A. T., Nasuno, T., & Iga, S. I. (2007). A short-duration global cloud-resolving simulation with a realistic land and sea distribution. *Geophysical Research Letters*, *34*(2), 2–6. https://doi.org/10.1029/2006GL027448

Pearson, K. J., Lister, G. M., Birch, C. E., Allan, R. P., Hogan, R. J., & Woolnough, S. J. (2014). Modelling the diurnal cycle of tropical convection across the 'grey zone'. *Quarterly Journal of the Royal Meteorological Society*, *140*(679), 491–499. https://doi.org/10.1002/qj.2145

Petch, J. C., Brown, A. R., & Gray, M. E. (2002). The impact of horizontal resolution on the simulations of convective development over land. *Quarterly Journal of the Royal Meteorological Society*, *128*(584), 2031–2044. https://doi.org/10.1256/003590002320603511

Peters, K., Hohenegger, C., & Klocke, D. (2019). Different representation of mesoscale convective systems in convection-permitting and convection-parameterizing NWP models and its implications for large-scale forecast evolution. *Atmosphere*, *10*(9), 1–18. https://doi.org/10.3390/atmos10090503

Pfeifroth, U., Mueller, R., & Ahrens, B. (2013). Evaluation of satellite-based and reanalysis precipitation data in the tropical Pacific. *Journal of Applied Meteorology and Climatology*, *52*(3), 634–644. https://doi.org/10.1175/JAMC-D-12-049.1

Prein, A. F., Gobiet, A., Suklitsch, M., Truhetz, H., Awan, N. K., Keuler, K., & Georgievski, G. (2013). Added value of convection permitting seasonal simulations. *Climate Dynamics*, *41*(9–10), 2655–2677. https://doi.org/10.1007/s00382-013-1744-6

Rayner, N. A., Parker, D. E., Horton, E. B., Folland, C. K., Alexander, L. V., Rowell, D. P., & Kaplan, A. (2003). Global analyses of sea surface temperature, sea ice, and night marine air temperature since the late nineteenth century. *Journal of Geophysical Research*, *108*(14), 4407. https://doi.org/10.1029/2002jd002670

Samanta, D., Karnauskas, K. B., & Goodkin, N. F. (2019). Tropical Pacific SST and ITCZ biases in climate models: Double trouble for future rainfall projections? *Geophysical Research Letters*, *46*(4), 2242–2252. https://doi.org/10.1029/2018GL081363

Satoh, M., Stevens, B., Judt, F., Khairoutdinov, M., Lin, S.-J., Putman, W. M., & Düben, P. (2019). Global cloud-resolving models. *Current Climate Change Reports*, *5*(3), 172–184. https://doi.org/10.1007/s40641-019-00131-0

Satoh, M., Tomita, H., Yashiro, H., Kajikawa, Y., Miyamoto, Y., Yamaura, T., et al. (2017). Outcomes and challenges of global high-resolution non-hydrostatic atmospheric simulations using the K computer. *Progress in Earth and Planetary Science*, *4*(1), 13. https://doi.org/10.1186/s40645-017-0127-8

Schär, C., Fuhrer, O., Arteaga, A., Ban, N., Charpilloz, C., Di Girolamo, S., et al. (2020). Kilometer-scale climate models: Prospects and challenges. *Bulletin of the American Meteorological Society*, *101*(5), E567–E587. https://doi.org/10.1175/BAMS-D-18-0167.1

Schneider, T., Bischoff, T., & Haug, G. H. (2014). Migrations and dynamics of the intertropical convergence zone. *Nature*, *513*(7516), 45–53. https://doi.org/10.1038/nature13636

Siongco, A. C., Hohenegger, C., & Stevens, B. (2015). The Atlantic ITCZ bias in CMIP5 models. *Climate Dynamics*, *45*(5–6), 1169–1180. https://doi.org/10.1007/s00382-014-2366-3

Siongco, A. C., Hohenegger, C., & Stevens, B. (2017). Sensitivity of the summertime tropical Atlantic precipitation distribution to convective parameterization and model resolution in ECHAM6. *Journal of Geophysical Research*, *122*(5), 2579–2594. https://doi.org/10.1002/2016JD026093

Slingo, J., Bates, P., Bauer, P., Belcher, S., Palmer, T., Stephens, G., et al. (2022). Ambitious partnership needed for reliable climate prediction. *Nature Climate Change*, *12*(6), 499–503. https://doi.org/10.1038/s41558-022-01384-8

Stevens, B., Acquistapace, C., Hansen, A., Heinze, R., Klinger, C., Klocke, D., et al. (2020). The added value of large-eddy and storm-resolving models for simulating clouds and precipitation. *Journal of the Meteorological Society of Japan*, *98*(2), 395–435. https://doi.org/10.2151/jmsj.2020-021

Wernli, H., Paulat, M., Hagen, M., & Frei, C. (2008). SAL - a novel quality measure for the verification of quantitative precipitation forecasts. *Monthly Weather Review*, *136*(11), 4470–4487. https://doi.org/10.1175/2008MWR2415.1

Wu, X., Liang, X. Z., & Zhang, G. J. (2003). Seasonal migration of ITCZ precipitation across the equator: Why can't GCMs simulate it? *Geophysical Research Letters*, *30*(15), 10–13. https://doi.org/10.1029/2003GL017198

Yang, G. Y., & Slingo, J. (2001). The diurnal cycle in the tropics. *Monthly Weather Review*, *129*(4), 784–801. https://doi.org/10.1175/1520-0493(2001)129<0784:TDCITT>2.0.CO;2